Continental Shelf Research 78 (2014) 51–61

Contents lists available at ScienceDirect

Continental Shelf Research

journal homepage: www.elsevier.com/locate/csr

Research papers

Properties of Red Sea coastal currents

J.H. Churchill [a,*], S.J. Lentz [a], J.T. Farrar [a], Y. Abualnaja [b]

[a] Department of Physical Oceanography, Woods Hole Oceanographic Institution, Woods Hole, MA 02543, USA
[b] Red Sea Research Center, King Abdullah University of Science and Technology, Thuwal, Saudi Arabia

ARTICLE INFO

Article history:
Received 28 March 2013
Received in revised form
23 January 2014
Accepted 28 January 2014
Available online 14 February 2014

Keywords:
Red Sea
Coastal flows
Basin-shelf interaction

ABSTRACT

Properties of coastal flows of the central Red Sea are examined using 2 years of velocity data acquired off the coast of Saudi Arabia near 22 °N. The tidal flow is found to be very weak. The strongest tidal constituent, the M_2 tide, has a magnitude of order 4 cm s^{-1}. Energetic near-inertial and diurnal period motions are observed. These are surface-intensified currents, reaching magnitudes of >10 cm s^{-1}. Although the diurnal currents appear to be principally wind-driven, their relationship with the surface wind stress record is complex. Less than 50% of the diurnal current variance is related to the diurnal wind stress through linear correlation. Correlation analysis reveals a classical upwelling/downwelling response to the alongshore wind stress. However, less than 30% of the overall sub-inertial variance can be accounted for by this response. The action of basin-scale eddies, impinging on the coastal zone, is implicated as a primary mechanism for driving coastal flows.

1. Introduction

Flows over coastal/continental shelf regions have been subject to numerous studies, owing largely to their commercial and ecological importance. However, while currents of some shelf areas have been extensively examined (as off the US and European coasts), very little is known about the flow dynamics in many of the world's coastal regions. Given that coastal flow is the product of a complex mix of factors (i.e. freshwater discharge, tides, wind forcing in various frequency bands and the influence of motions imposed from the open ocean), coastal dynamics may be regarded as distinctly regional, and the findings from well-studied coastal regions may not be applicable to other areas.

Here we present the first analysis of flow properties over a coastal area of the central Red Sea, utilizing data acquired over 2008–2010 from moored instruments and a meteorological buoy. Employing standard statistical techniques, we examine the character of the surface wind stress, the local flow response to the wind and the tidal motion. We also consider the forcing of coastal flow by basin-scale eddies impinging on the coastal zone. This work is intended to form the basis of more in-depth studies of particular aspects of the coastal flow dynamics and of the coupled physical–chemical–biological coastal system of the central Red Sea.

2. Site description

The region of study is a shallow (30–90 m deep) plateau off the western coast of Saudi Arabia, between Jeddah and King Abdullah University of Science and Technology (Fig. 1). In the north–south (along-shore) direction it extends over roughly 30 km, bounded to the north by the Abu Madafi reef and to the south by the Eliza Shoals reef system. In the east–west direction it extends over roughly 10 km, from the edge of the Red Sea basin to the Qita Dukais reef system. Bathymetry data acquired for mooring site selection show that the bottom slope just seaward of the plateau is extremely steep, typically order 1 (i.e., a 500 m drop over 500 m horizontal distance) and >2 over some sections. The depth data also reveal that the plateau bottom is studded by numerous sharply crested features, presumably coral heads, with heights of 0.5–5 m. The bathymetric complexity of this region is typical of Red Sea coastal areas, which are dominated by reef and island formations.

3. Methods

The oceanographic data used in our study come from two mooring deployments, each extending over roughly 13 months. In the first (mid-October 2008 to mid-November 2009), measurements were acquired at two closely spaced sites, designated S1 and S2 (Fig. 1). The instrumentation deployed at each site included a bottom tripod outfitted with an upward-looking Teledyne RDI Sentinel Acoustic Doppler Current Profiler (ADCP) and a SeaBird

* Corresponding author. Tel.: +1 508 289 2807.
E-mail addresses: jchurchill@whoi.edu (J.H. Churchill), slentz@whoi.edu (S.J. Lentz), jfarrar@whoi.edu (J.T. Farrar), yasser.abualnaja@kaust.edu.sa (Y. Abualnaja).

http://dx.doi.org/10.1016/j.csr.2014.01.025

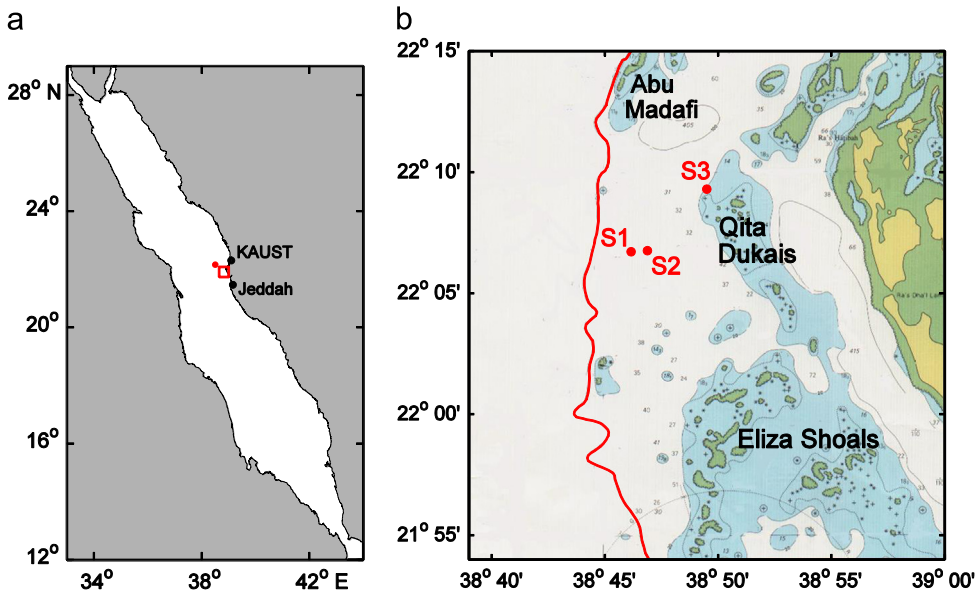

Fig. 1. (a) Large-scale map of the Red Sea showing the location of the meteorological buoy (red circle) from which our wind and heat flux measurements were derived. (b) Locations of the study's moorings superimposed on a bathymetric map (United Kingdom Hydrographic Office) of the area outlined by the box in (a). The red line traces the 100-m isobath, marking the eastern edge of the Red Sea basin.

Seagauge pressure sensor, as well as an array of Onset TempPro temperature sensors (Lentz et al., 2013) and SeaBird MicroCat temperature/conductivity sensors attached to a wire mooring supported by a surface buoy. Unfortunately, no data were recovered from the instruments on the S1 mooring line, as its surface buoy detached in June 2009. S1 and S2 were at roughly 55-m depth on the outer/mid-plateau and, respectively, 2.5 and 3.5 km from the plateau's seaward edge. Our intent had been to deploy one mooring/tripod pair near the plateau-edge and the other at the mid-plateau. However, the rugged, coral-encrusted sea floor, and the requirement that the tripods be deployed on a nearly flat bottom, limited our deployment site options.

In the second deployment (mid-November 2009 to mid-December 2010) measurements were acquired at S2 and at an inner plateau site, S3. The latter was near the seaward edge of the Qita Dukais reef system, at a water depth of 38 m, and roughly 8 km from the plateau's seaward edge (Fig. 1). A mooring/tripod pair, outfitted as in the first deployment, was deployed at each site. To avoid mooring ground line fouling on bottom coral, which may have been responsible for the S1 buoy detachment, the moorings of the second deployment were each supported by a sub-surface buoy (i.e., taut-wire moorings).

For both deployments, the ADCPs were programmed to give 4–5 min burst-averaged velocities at 0.5 h intervals. The velocities were vertical averages over bins of either 0.5 (S3) or 1 m (S1 and S2). The measurement bins extended from 2–4 m above the seafloor to 4–6 m below the surface. The near-surface velocity records from the 600-kHz ADCP set out at S2 during the first deployment had numerous gaps due to the range limitation of the ADCP. This was not an issue for the velocity record from the longer-ranged 300-kHz ADCP set out at S1. Analysis of first deployment flows shown here focuses on the velocities from S1.

Temperature measurements spanned the water column at each site, extending from less than 1 m above the bottom to within 0.6 m of the surface during the first deployment and to ~4 m from the surface during the second deployment. Vertical separation of temperature measurements was 4 m or less. MicroCats provided salinity measurements at 5–6 depths spanning the water column. Samples were taken every 15 min by the TempPros and every 150 s by the MicroCats. Seagauges recorded 1-min averages of near-bottom pressure. All velocity, temperature, salinity and pressure time series were linearly interpolated to a common time base with a 1 h interval.

Meteorological data used in our study came from an Improved Meteorological (IMET) sensor suite installed on a surface buoy deployed in the Red Sea basin at a water depth of roughly 700 m and at a location 36.5 km northwest of S1 (Fig. 1). The IMET measurements included wind speed and direction, air temperature, relative humidity, barometric pressure, incoming shortwave radiation and longwave radiation (Hosom et al., 1995; Payne and Anderson, 1999; Colbo and Weller 2009). Surface wind stress and heat flux were estimated from the meteorological data using the bulk formulae of Fairall et al. (2003).

Our study included analysis of altimeter-derived sea level anomaly (SLA) fields computed with respect to the CLS01 (Center de Localization d'Satellittes) long-term mean sea surface height. The fields were obtained from AVISO (http://www.aviso.oceanobs.com/) and combine the data of all available satellites in an objectively mapped grid of SLA with 0.25° grid spacing. The gridded SLA fields were used to estimate fields of geostrophic surface velocity through

$$u_G = \frac{g}{f}\frac{\partial \delta}{\partial y};\ v_G = -\frac{g}{f}\frac{\partial \delta}{\partial x}$$

where δ is SLA, u_G and v_G are, respectively, the east and north components of geostrophic velocity, g is the gravitational acceleration and f is the local Coriolis parameter.

The statistical methods used to analyze the velocity series included rotary spectral analysis and complex demodulation. Rotary spectral analysis is used to divide the flow's energy density within frequency bands into circularly rotating clockwise, S_+, and counterclockwise, S_-, constituents (Gonella, 1972). Rotary spectra have been used to distinguish the signal of inertial currents, which move in a nearly circular clockwise path in the northern hemisphere, from a tidal signal, which typically has both clockwise and counterclockwise components (Gonella, 1972). The polarization of the flow in a frequency band is described by the rotary coefficient, $CR=(S_- - S_+)/(S_- + S_+)$, which varies from 1 for pure circular flow to 0 for unidirectional flow.

Complex demodulation involves applying a Fourier transform centered at a frequency of interest to short segments of a velocity

time series. For each segment, the transform gives an estimate of the amplitude of the motion at the selected frequency (see Perkins, 1976). The transform is stepped through the velocity series to give a time series of the estimated amplitude of the motion at the selected frequency. In generating the results shown here, the transform length was set to twice the period of the signal of interest (i.e., to 48 h for demodulation targeting the diurnal signal).

A time series filter was employed to extract low and high frequency, as well as band-passed, signals from the velocity records. The filter, commonly referred to as the Pl66 filter (Limeburner, 1985), is a low-pass filter characterized by a half-power period.

To estimate the properties of the tidal flow, we applied harmonic analysis to the velocity series using a MATLAB routine, t_tide (Pawlowicz et al., 2002). For up to 67 tidal constituents, this routine estimates the velocity magnitude along principal axes of the tidal ellipse as well as the ellipse orientation.

4. Results

4.1. Water column structure

The vertical density stratification is of importance when considering the vertical distribution of wind-driven currents, as the stratification influences the downward transfer of momentum imparted at the sea surface (e.g., Price et al., 1986). As revealed by the CTD data from mooring S2, the temporal variation of the vertical density stratification, ρ_z, in our study area has a well-defined seasonal signal, which is repeated over our two study years. This signal is related to the vertical temperature stratification, T_z, which is in turn related to the surface heat flux, H (Fig. 2). In general terms, this signal can be divided into three periods: April–August, when T_z and ρ_z tend to increase and the mean H is order 75 W m^{-2} (directed into the sea); September–October, when T_z and ρ_z tend to decline and the mean H is near zero; and November–March, when T_z and ρ_z are predominately weak and the mean H is order -100 W m^{-2} (Fig. 2). Intermittent episodes of relatively strong T_z and ρ_z, persisting for a number of days, are observed during this last period. Most occur in February–March, and are likely due to surface warming as they coincide with episodes in which the low-pass filtered (50-hr half-power period) H is positive (Fig. 2).

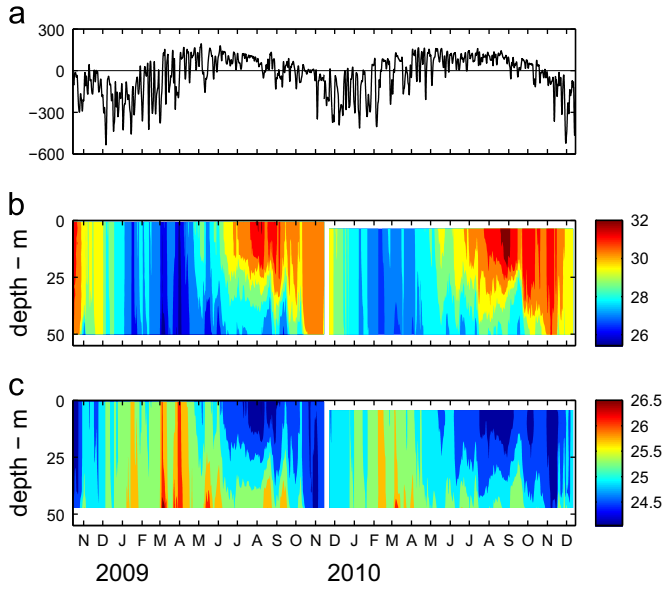

Fig. 2. Low-pass (50-hr half-power period) filtered surface heat flux (a, in W m^{-2}) together with contoured (over time and depth) low-pass (also 50-hr half-power period) filtered temperature (b, in °C) and density (c, in σ_T) measured at site S2 (Fig. 1). As noted in the text, temperature and density stratification exhibit a seasonal cycle, which is related to the surface heat flux.

Episodes of relatively strong vertical salinity stratification are also observed. These are typically due to the appearance of high salinity (>39.4 psu) bottom water, which results in a vertical salinity range of order 0.5 psu (and never >1 psu).

Superimposed on the seasonal signal of T_z and ρ_z described above are diurnal T_z and ρ_z variations associated with the formation of a surface warm layer due to solar heating. These diurnal warm layers are seen during all seasons. Over November–March they appear within a weakly stratified, or unstratified, water column, whereas during April–October they are embedded within the evolving seasonal stratification (Fig. 3). Their properties are highly variable, reflecting the complex interaction between surface heating and wind-induced vertical mixing (e.g., Kondo et al., 1979; Price et al., 1986; Woods and Strass, 1986; Fairall et al., 1996; Noh et al., 2011). As represented by the examples shown here (Fig. 3), the depth of the diurnal warm layer as seen at S2 varies considerably, roughly between 2 and 20 m. The near-surface (0.6 m) diurnal temperature signal (difference between the daytime maximum and nighttime minimum) is typically in the range of 0.2–1 °C (for 78% of the days) and occasionally exceeds 2 °C (for 1% of the days).

4.2. Character of the central Red Sea winds

Analysis of the Comprehensive Atmosphere-Ocean Data Set (COADS) by Sofianos and Johns (2001) revealed that the wind component directed along the axis of the Red Sea may be divided into two distinct regimes. Along-axis winds over the southern Red Sea ($<19^\circ$ N) undergo a seasonal reversal, being predominately to the NNW (from the SSE) from October through May and to the SSE from June through September. By contrast, along-axis winds over the northern Red Sea are predominately to the SSE throughout the year. A recent study by Jiang et al. (2009) focused on the Red Sea's across-axis wind field resulting from the atmospheric flows steered through the coastal mountain gaps. Their modeling results for the northern Red Sea (north of 20° N) reveal a tendency for such flows to produce bands of strong westward wind, principally during the late autumn and winter.

The along-axis (NNW-SSE) winds measured at our meteorological buoy tend to conform with the northern wind regime pattern described by Sofianos and Johns (2001). Except for very occasional reversals, the along-axis wind is predominately directed to the SSE (from the NNW) (Figs. 4 and 5). As described by Jiang et al. (2009), the wind record also shows occasional episodes of strong (stress >0.15 Pa) winds directed offshore (to the WSW). These are confined to the months of November–January.

The tendency for the wind to be directed along the Red Sea axis is indicated by the basic wind statistics. For both deployments, the mean wind stress is directed to the SSE, within 2° of 147° T (clockwise of N), and the major principal axes of the low-pass filtered (with 50-h half-power period) wind stress records are oriented along the SSE-NNW line (along ~145° T; Fig. 5, Table 1). The low-frequency wind stress is highly polarized. The ratio of the minor to the major principal axes of the low-pass filtered wind stress record is order 0.5, and the rotary coefficients of the wind stress in the 1.7–42.7 d spectral band are order 0.1 (Table 1).

Wind stress spectra exhibit prominent peaks at periods of 12 and 24 h (Fig. 6), evidence of a vigorous sea breeze. The sea breeze accounts for an appreciable portion of the overall wind energy. The variance of the wind stress in what may be considered the sea breeze band (11.5–34.1 h period) comprises 21% and 26% of the overall wind stress variance of deployments 1 and 2, respectively.

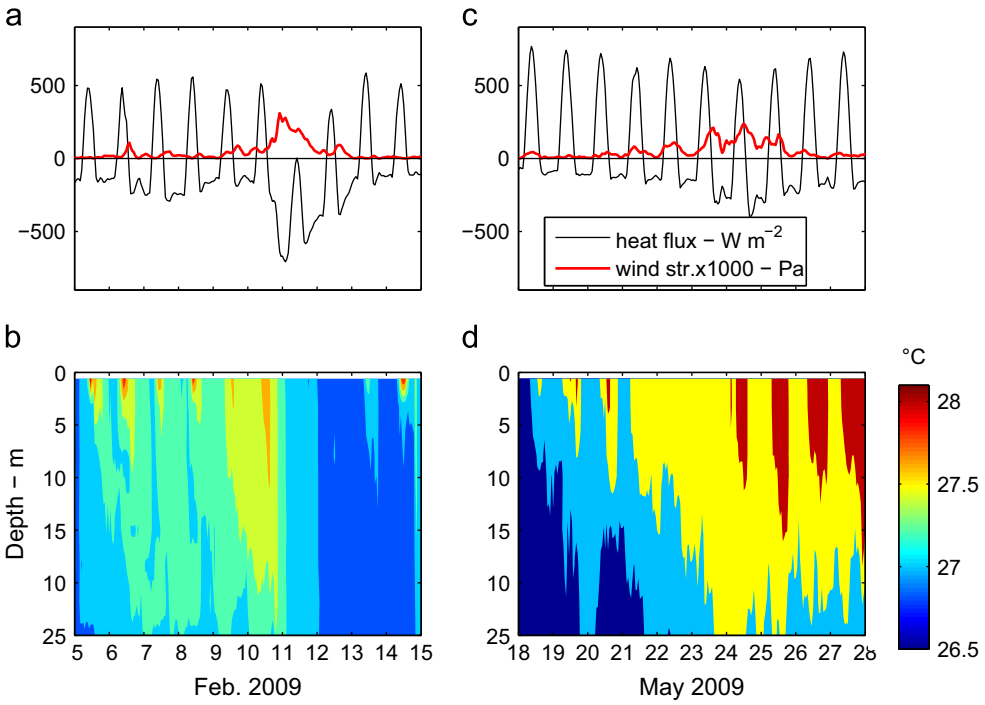

Fig. 3. The lower panels (b and d) show 10-day segments of the temperature signal measured at site S2, which clearly reveal the formation of near-surface diurnal warm layers. The upper panels (a and c) show the surface heat flux and wind stress measured at the offshore meteorological buoy. The warm layer formation is clearly associated with positive (into the sea) heat flux.

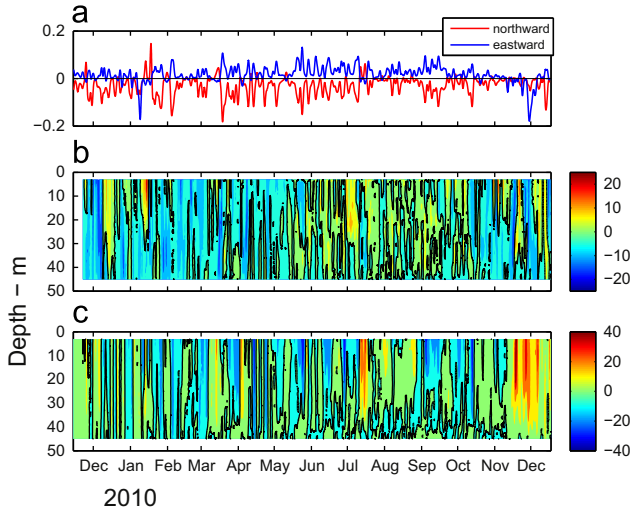

Fig. 4. Low-pass (50-hr half-power period) filtered surface wind stress (a, in Pa) together with contoured low-pass filtered eastward and northward velocities (b and c, in cm s^{-1}) measured at S2 during the second mooring deployment.

Similar to the low-frequency winds, sea breeze winds are polarized, as indicated by the 0.25–0.5 rotary coefficients of the semidiurnal (11.5–13.0 h periods) and diurnal (22.7–25.6 h) bands of the wind stress rotary spectra (Table 1). The major principal axis of both the semidiurnal and diurnal wind stress signals (determined by band-pass filtering the wind stress series with filters roughly centered at periods of 12 and 24 h) are closely aligned with ESE-WNW.

To give a sense of how the wind stress varies over the course of a day, we have averaged the wind stress records of the first and second deployments over each hour of the day. Here we present hour-of-the-day wind stress averages of the second deployment along the diurnal wind stress principal axes directions (Fig. 7). For all hours of the day, the averaged wind stress along the major axis is directed shoreward (to 118° T). It exhibits more than a 4-fold variation, increasing from a minimum of 0.013 Pa at midnight to a maximum of 0.064 Pa at 17:00 (local time). The averaged wind stress along the minor axis exhibits a relatively weak semidiurnal signal with maximum magnitudes occurring at 8:00 and 20:00.

4.3. General character of the measured flows

The mean water velocities, averaged over depth and each mooring period, are relatively weak, not greater than 2.2 cm s^{-1} (Table 2). They are not aligned with the mean wind stresses of the deployment periods (Fig. 5). Mean velocity orientations of the second deployment period are nearly opposite the mean wind orientation. The implication is that the forcing of the mean velocities includes factors other than the surface wind stress, with some combination of along- and across-shore pressure gradients likely being important.

The low frequency currents are highly polarized. The ratio of the minor to major principal axes of the depth-averaged, low-pass (50-h half-power period) filtered current records of each deployment is of order 0.4 (Fig. 5) and the rotary coefficients of these records in the 1.7–42.7-d band range over 0.08–0.30 (Table 2). The major principal axes of the depth-averaged, low-pass filtered currents from S1 and S2 are closely aligned (within 7°) of the N–S direction. For this reason, we have chosen the N–S axis as the along-shore direction of the mid-plateau flows. The major principal axis of the low-pass filtered, depth-averaged current at S3 is not as closely aligned with N–S, offset by 13°. This is likely due to the influence of the local bathymetry at S3, which was located at the edge of the Qita Dukais reef system (Fig. 1).

Near-surface spectra of velocities from all sites exhibit three distinct peaks at periods of <2 d (e.g., Fig. 8a). One is seen near the local inertial frequency, f (the inertial period at the study latitude, ~22° N, is 32 h), and the others are at the diurnal and

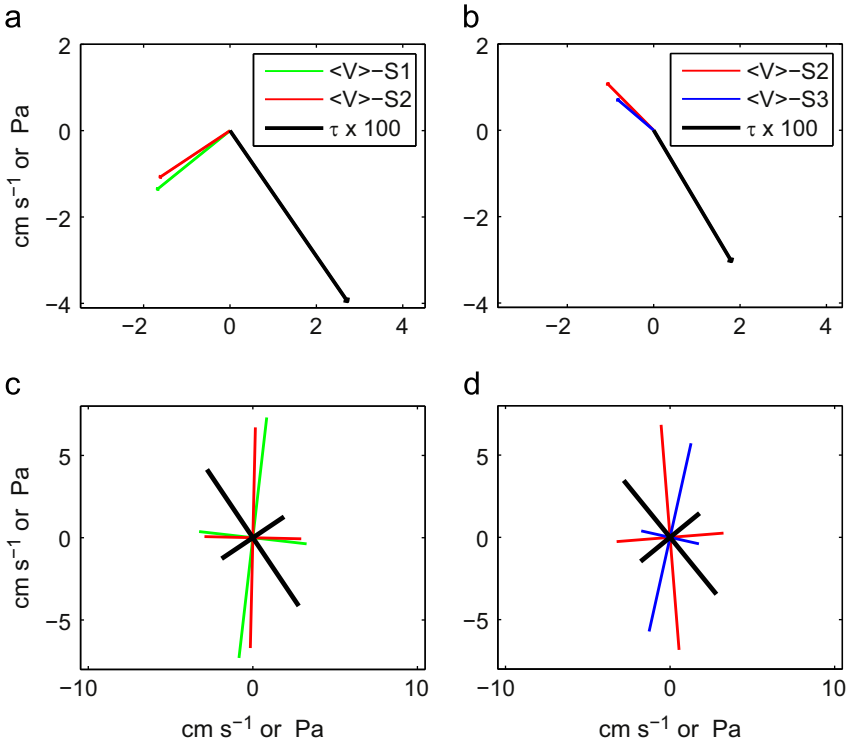

Fig. 5. Means (a and b) and principal axes (c and d) of the surface wind stress (τ) and depth-averaged velocities ($<V>$) at the indicated mooring sites for the first (a and c) and second (b and d) mooring deployment.

Table 1
Properties of the surface wind stress records, as determined from rotary spectral analysis, of the first and second mooring deployment.

	Deployment 1	Deployment 2
Date range	10/12/2008-11/14/2009	11/27/2009-12/18/2010
Mean $[\tau_y,\tau_y]$ (Pa) × 100	2.7, −4.0	1.8, −3.0
Sub-inertial; 1.7–42.7 days		
Variance (Pa^2) × 10^4	34.0	26.7
Rotary coefficients	0.12	0.03
Diurnal; 22.7–25.6 h		
Variance (Pa^2) × 10^4	4.0	3.8
Rotary Coefficients	0.50	0.26
Semidiurnal; 11.5–13 h		
Variance (Pa^2) × 10^4	1.3	1.5
Rotary coefficients	0.48	0.47
D-SD band; 11.5–34.1 h		
Variance (Pa^2) × 10^4	9.1	9.9
Rotary coefficients	0.41	0.27

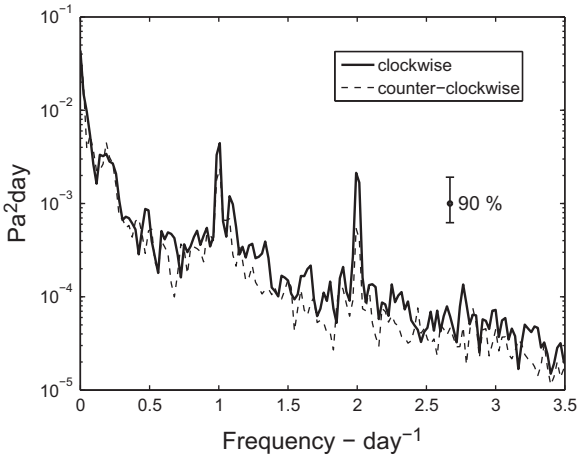

Fig. 6. Rotary spectra of the surface wind stress at the meteorological buoy (Fig. 1a) for the second mooring deployment. Prominent peaks appear at the diurnal and semidiurnal frequencies.

semidiurnal frequencies. Notably, the inertial and diurnal frequency peaks, which are both predominately in the clockwise spectra, are separated by a spectral valley. The energy at the inertial and diurnal frequencies declines with increasing depth. The spectral peaks at these frequencies are significantly reduced, relative to the peaks of the surface current spectra, in the spectra of the mid-depth currents, and they are essentially absent from the spectra of near-bottom currents (Fig. 8). By contrast, the spectral peak of currents at the semidiurnal frequency is reduced with depth, but is still prominent in the spectra of the near-bottom currents.

To assess the relative contribution of the inertial-, diurnal- and semidiurnal-band velocity fluctuations to the overall current variance, we have summed the variance in these bands of depth-averaged and near-surface currents (Table 2). For depth-averaged flows, the variance in the semidiurnal-band is 2–3 times the variance in the diurnal and inertial bands. For near-surface flows, however, the variances in all bands are comparable. For both depth-averaged and near-surface currents, variance in the sub-inertial band (1.7–42.7 d periods) overshadows the variance in the inertial, diurnal and semidiurnal bands by an order of magnitude. However, the combined variance in the band encompassing the inertial, diurnal and semidiurnal frequencies (11.5–34.1 h periods) is roughly 1/3 the variance in the sub-inertial band at S1 and S2 and 1/2 the sub-inertial band variance at S3. Below, we separately examine the properties of the near-inertial, diurnal and semidiurnal flows, after first examining the properties of the tidal currents.

4.4. Results of harmonic tidal analysis

Analyses of sea surface elevation data, reviewed by Morcos (1970), show a small tidal range (<0.25 m) over the central Red Sea ($\sim$19–24° N) as well as an amphidromic point of the M_2 tide at roughly 20° N. To estimate the strength of the barotropic tidal flow in our study region, we applied tidal harmonic analysis to the depth-averaged current records. The results (Table 3) indicate that the tidal flow at our study site is weak. Estimated velocity along the major principal axis exceeds 1 cm s^{-1} for only 4 constituents: S_1 (24-h period), N_2 (12.66 h), M_2 (12.42 h) and S_2 (12 h). The estimated M_2 velocities are the strongest, with 3.6–4.1 cm s^{-1} magnitudes along the major axis. Estimated flows of the other two semidiurnal tides, N_2 and S_2, are considerably weaker, with 1.1–1.5 cm s^{-1} along-major-axis magnitudes. Estimated flows of the diurnal, S_1, constituent are particularly weak, with along-major-axis magnitudes of <1.3 cm s^{-1}. These tidal velocity estimates are probably slightly greater than the actual tidal velocities, as the harmonic analysis is likely contaminated by flows driven by the diurnal and semidiurnal wind stress signals. We conclude that the flows of our study area include a weak semidiurnal tide and a negligible contribution from the diurnal tide.

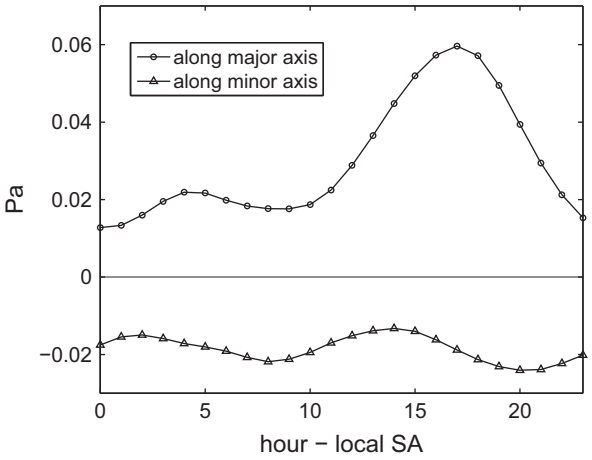

Fig. 7. Wind stress of the second mooring deployment averaged over hour of the day. The averages shown are along the major and minor principal axes (toward 118 and 28° T, respectively) of the diurnal wind stress signal.

4.5. Near-inertial currents

Rotational currents with a peak frequency near the local inertial frequency have been observed in a number of coastal velocity records (e.g., Schumann and Perrins, 1982; Chen et al, 1996; Chant, 2001; Shearman, 2005) and often have been linked to strong wind events (Kundu, 1976; Chant, 2001; Lerczak et al., 2001). The near-inertial currents observed in all ADCP records show a decline with increasing depth, with the rate of decline related to the vertical temperature stratification. In the example shown here (Fig. 9), the inertial-band variance from the top to the base of the ADCP measurement range declines by a factor of 4 over a 3.5-month period when the water column is nearly unstratified, but lessens by a factor of nearly 30 (to essentially 0 near the bottom) over a 3.5-month period of strong vertical temperature stratification. For the latter period, the decline in inertial-band variance is greatest over the depth range with the strongest vertical temperature and density gradient (15–30 m). The time series of near-surface inertial-band current magnitude, estimated by complex demodulation, exhibits a number of distinct peaks with amplitudes ranging from roughly 5 to 15 cm s^{-1} (Fig. 10). In general, the highest peaks (i.e. the strongest near-surface inertial-band currents) occur during the April–October period of persistent vertical temperature and density stratification (Fig. 2).

Examination of the wind stress and inertial-band current magnitude time series have revealed no clear relationship between wind stress and the onset of strong inertial currents (Fig. 10). For example, strong inertial currents are sometimes observed in periods of weak winds following a strong wind stress event, and sometimes are not. This inconsistency is not related to vertical temperature stratification, as it occurs during times of weak and strong stratification.

4.6. Diurnal-band currents

Diurnal-band currents tend to rotate in a clockwise direction (Fig. 8) and are more weakly polarized than diurnal-band winds, which have rotary coefficients of 0.25–0.5 as opposed to the order

Table 2
Properties of the depth-averaged and near-surface flows, as determined from rotary spectral analysis, of the first and second deployment (D1 and D2). The period range of each motion type is: sub-inertial 1.7–42.7 d; inertial 27.7–34.1 h; diurnal 22.7–25.6 h; semi-diurnal 11.5–13.0 h; I-D-SD band 11.5–34.1 h. Means and variances have units of cm s^{-1} and cm^2 s^{-2}, respectively.

	Depth-averaged flows			Near-surface flows		
	S1–D1	S2–D2	S3–D2	S1–D1 (6.5 m)	S2–D2 (3.0 m)	S3–D2 (6.2 m)
Date range	10/12/2008–11/14/2009	11/27/2009–12/18/2010	11/27/2009–12/18/2010	10/12/2008–11/14/2009	11/27/2009–12/18/2010	11/27/2009–12/18/2010
Mean [u,v]	−1.7, −1.4	−1.1, 1.1	−0.9, 0.9	−2.5, −5.3	0.4, −1.1	−0.9, 0.2
Sub-inertial						
Variance	62.7	63.3	44.1	199.2	169.3	124.8
Rotary coefficients	0.30	0.16	0.08	0.32	0.09	0.04
Inertial						
Variance	4.1	4.1	5.5	18.8	16.2	19.2
Rotary coefficients	0.64	0.76	0.51	0.77	0.78	0.52
Diurnal						
Variance	3.1	3.5	2.8	15.8	14.9	13.1
Rotary coefficients	0.71	0.75	0.69	0.71	0.61	0.79
Semi-diurnal						
Variance	10.6	10.9	15.6	16.9	15.7	35.3
Rotary coefficients	0.54	0.49	0.64	0.68	0.61	0.64
I-D-SD band						
Variance	21.0	21.4	27.4	66.5	61.5	82.6
Rotary coefficients	0.56	0.60	0.60	0.64	0.59	0.57

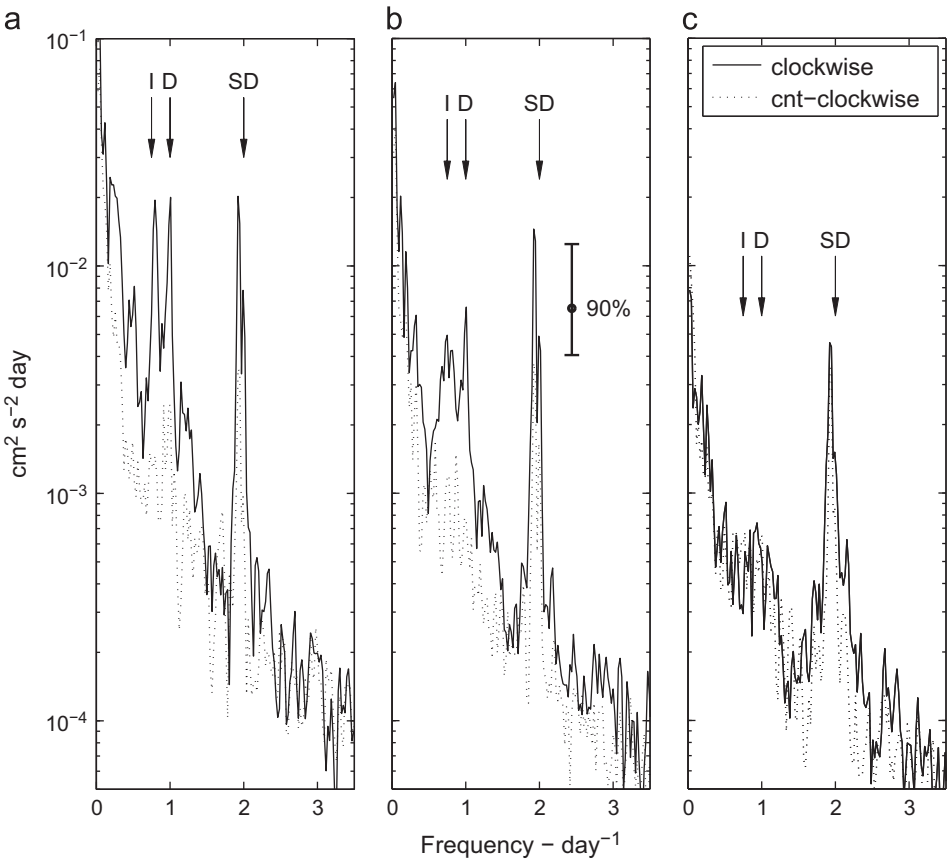

Fig. 8. Rotary spectra of currents measured at three depths (a - 6.5 m, b - 26 m, c - 48 m) at mooring S1 during the first mooring deployment. The semidiurnal (SD), diurnal (D) and local inertial (I) frequencies are indicated.

Table 3
Estimated properties of the S_1 (24 h), N_2 (12.66 h), M_2 (12.42 h) and S_2 (12 h) tidal flows as determined by harmonic analysis of the depth-averaged velocity series.

Mooring/ Deployment	Constituent	Major axis velocity cm s^{-1}	Minor axis velocity cm s^{-1}	Major axis orientation °T
S1/D1	S_1	1.0	0.7	353
	N_2	1.1	0.2	338
	M_2	3.6	1.0	339
	S_2	1.5	0.4	327
S2/D2	S_1	1.3	1.0	338
	N_2	1.2	0.3	328
	M_2	3.7	0.9	336
	S_2	1.4	0.4	327
S3/D2	S_1	1.2	0.8	21
	N_2	1.4	0.6	341
	M_2	4.1	1.7	345
	S_2	1.4	0.5	342

0.7 rotary coefficients of diurnal-band currents (Tables 1 and 2). Similar to variance of near-inertial currents, diurnal-band current variance declines with increasing depth, with the rate of decline tending to be greatest over depths with strong vertical temperature stratification (Fig. 9). Time series of the diurnal-band current magnitude show a number of distinct peaks (Fig. 10), which tend to reach higher values during times of vertical temperature stratification. The most prominent peak occurs in August 2009, but does not coincide with unusually high total wind stress magnitude, or with unusually high diurnal wind stress magnitude (not shown) as computed by complex demodulation.

To quantify the relation of diurnal-band winds and near-surface currents, we carried out a lagged correlation analysis relating the band-pass filtered (with a filter centered at 24-h period) series of wind stress and near-surface velocity, each directed along their major principal axis orientation. Correlation coefficients were calculated for entire deployment periods, and for sub-periods with strong and weak vertical temperature stratification. The correlation coefficients relating wind stress and currents during periods of strong stratification have maximum values at lags of 0–5 h (with wind stress leading) in the range of 0.47–0.57. These are appreciably greater than maximum coefficients of weakly stratified periods, which are 0.2–0.32. Similar results were obtained by correlating diurnal-band current and wind stress amplitude, as determined by complex demodulation. It must be emphasized that although the coefficients listed above are all significantly different from zero at the 95% confidence level, they indicate that a significant fraction of the diurnal-band current variance ($>50\%$) cannot be related to the wind stress through a linear correlation model.

4.7. Semidiurnal-band currents

In all velocity spectra, the peak within the semidiurnal band (11.5 to 13-h periods) is centered at the frequency of the M_2 tidal current (12.42-h period) (Fig. 8). The variance levels at 0.5 d^{-1} frequency, which include contributions from the S_2 tide and flows driven by the semidiurnal wind stress, are considerably less than at the M_2 frequency. To illustrate this point, we consider spectra of current records determined by averaging spectra computed over 1024-h segments (9 for each current record). For all such spectra, the energy level in the M_2 band appreciably exceeds the energy levels in the band centered at 0.5 d^{-1} (the S_2 band), which is separated from the M_2 band by two spectral bands. The ratio of the

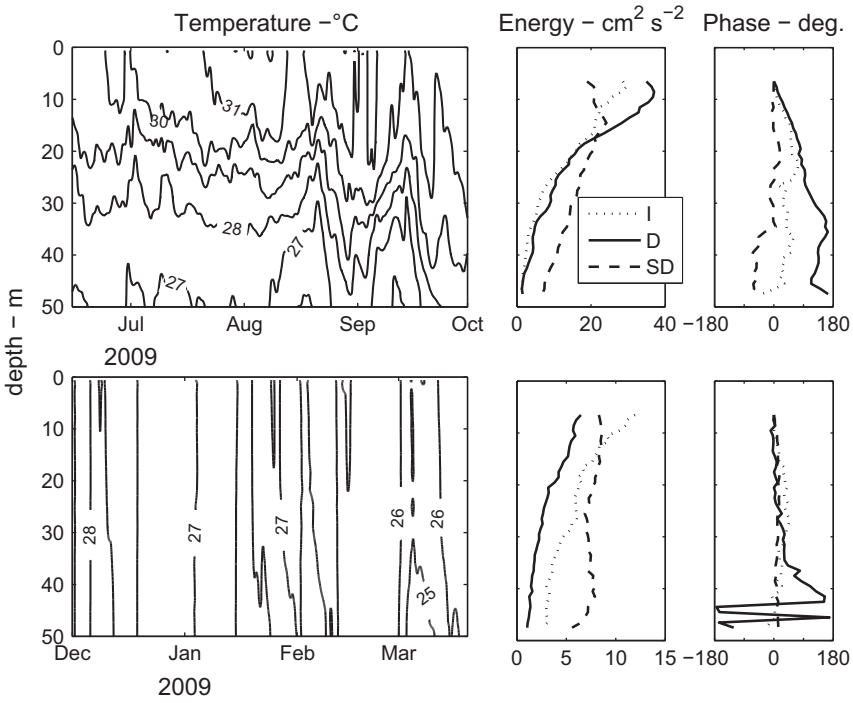

Fig. 9. The two right-most panels show the energy (total velocity variance) and phase (relative to the most near-surface velocity record) of the inertial (I, 27.7–34.1 h periods), diurnal (D, 22.8–25.6 h) and semidiurnal-M_2 (SD, 12.2–12.8 h) band velocities for the time periods encompassed by the contoured temperature fields shown in the left-most panels. The energy and phase profiles were determined from co- and cross-spectra of the velocity series.

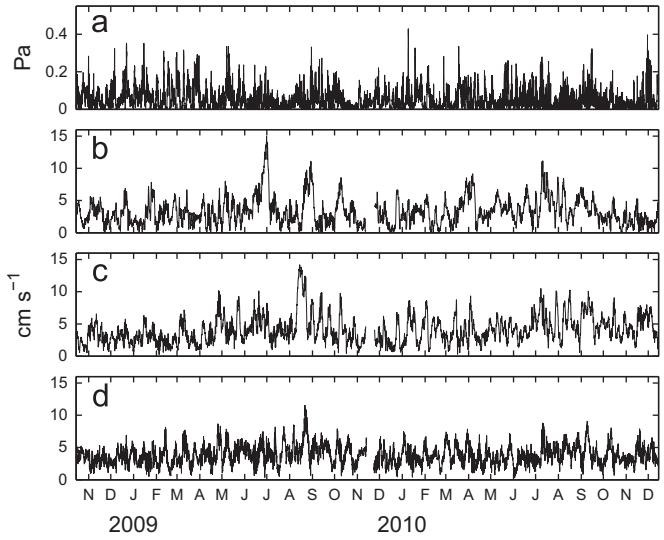

Fig. 10. Amplitudes (determined by complex demodulation) of near-surface inertial (b), diurnal (c) and semidiurnal (d) currents together with the magnitude of the surface wind stress (a).

M_2- to S_2-band energy increases going from the mid to the inner plateau, ranging over 2–7 in spectra computed from the S1 and S2 velocity records and over 5–9 in spectra computed from the S3 velocity records. This trend is consistent with the increasing strength of M_2 flow going from the mid to inner plateau as indicated by the results of tidal harmonic analysis (Table 3) and by the semidiurnal-band variances of the depth-averaged velocities (Table 2), which are ~1.5 times greater at S3 than at S1 or S2.

During periods of weak vertical temperature stratification, the semidiurnal-band (centered at the M_2 frequency) current signal exhibits the characteristics of a barotropic tide, with current variance and phase nearly homogeneous over the water column (Fig. 9). This contrasts with the downward decline of the diurnal-band current variance during times of weak stratification, consistent with the notion that diurnal-band flows are not appreciably influenced by tidal motions. However, during times of strong vertical temperature stratification, the variance and phase of semidiurnal-band currents vary considerably through the water column, possibly reflecting the influence of wind-driven flow or a baroclinic tidal contribution.

The amplitude of the near-surface, semidiurnal-band current signal (Fig. 10) is relatively small, seldom exceeding 8 cm s^{-1} and with a mean of 4 cm s^{-1}, consistent with tidal harmonic analysis of the velocity time series (Table 3).

4.8. Sub-inertial motions

Contoured (over depth and time) low-pass filtered (50-h half-power period) velocities reveal complex sub-inertial flow in the study region that is not clearly related to the low-pass filtered wind stress record through visual inspection (Figs. 4 and 11). Lagged correlation analysis was carried out to quantify the relationship between sub-inertial wind stress and water velocity. Here we focus on the results of the correlations relating the east (u, across-shore) and north (v, along-shore) velocity components with the north (τ_y, along-shore) wind stress. Maximum correlations occur at a lag of roughly 0 h for the τ_y–u correlation and at roughly 12 h for the τ_y–v correlation. Correlations at these lags show a consistent pattern for all velocity records from the mid-plateau sites S1 and S2 (Fig. 12). The τ_y–v correlation coefficients computed from these records are positive at all depths and in the range of 0.30–0.52 (statistically different from 0% at 95% confidence) over the upper 40 m. The τ_y–u correlation coefficients determined from the mid-plateau records reverse sign with depth, going from roughly 0.3 in the upper water to −0.3 in the lower water column. These extremes are significant at the 95% level. This correlation pattern is consistent with the classical response of

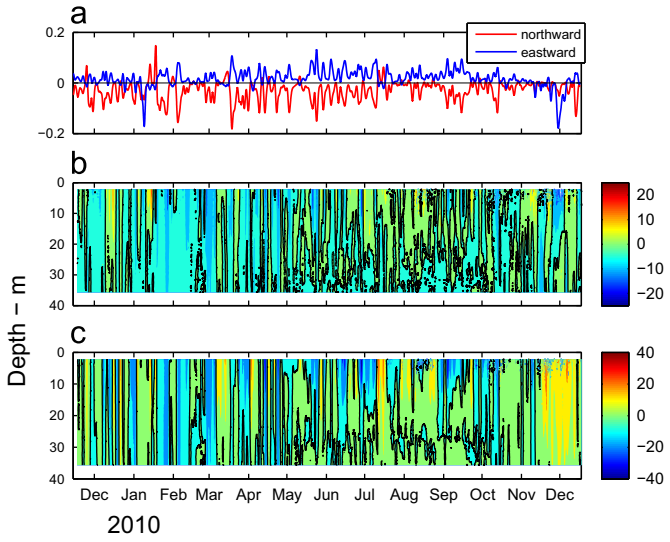

Fig. 11. Same as Fig. 4 except showing low-pass filtered velocities from S3.

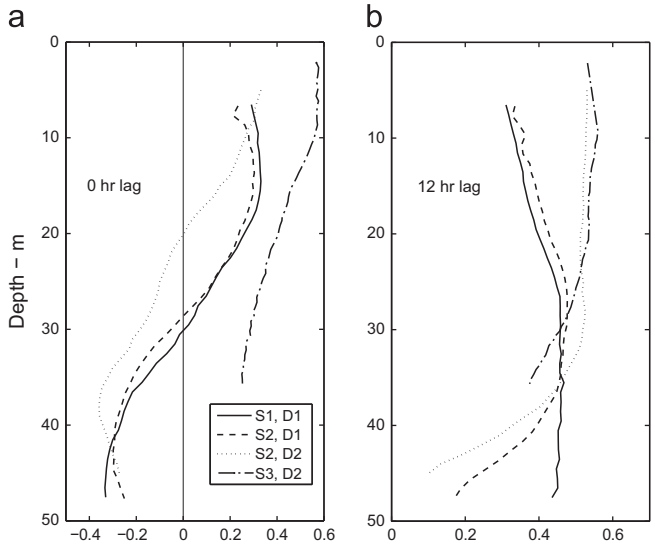

Fig. 12. Results of lagged correlation analysis relating the low-pass filtered (50-hr half-power period) northward (alongshore) surface wind stress with the low-pass filtered eastward (a) and northward (b) velocities measured over the indicated deployment (D#) and at the indicated mooring (S#).

coastal flow to along-shore wind stress forcing in the northern hemisphere, in which the along-shore flow is accelerated downwind (positive τ_y–v correlation) and the across-shore flow is directed to the right of the wind (positive τ_y–u correlation) near the surface and to the left of the wind (negative τ_y–u correlation) near the bottom. Similar correlation patterns of wind stress with water velocity, indicative of this "upwelling/downwelling" response to the alongshore wind stress, have been observed in other coastal areas (Smith, 1981; Beardsley et al., 1985; Churchill, 1985; Winant et al., 1987). We conclude that some fraction of the flow at the mid-plateau sites is driven by the alongshore wind stress in this classical pattern. However, this fraction is relatively small as the τ_y–u,v correlations, although statistically significant, are predominantly <0.5. The velocity variance accounted for by these correlations is thus less than 30% of the overall sub-inertial velocity variance.

The correlation analysis indicates that the northward (alongshore) flow at the inner-plateau site, S3, responds to the northward wind in a manner similar to that observed at the mid-plateau sites. The τ_y–v correlation coefficients computed from the S3 velocity records are positive at all depths and in the range of 0.37–0.56 (Fig. 12). However, the τ_y–u correlation coefficients determined from the mid-plateau and inner-plateau velocities are noticeably different. The coefficients determined from the inner-plateau velocities are positive at all depths and thus show no indication of an upwelling/downwelling response of the eastward flow to the alongshore wind. We speculate that the difference in wind-driven flows at the mid- and inner-plateau sites may be due to the topographic influence of the Qita Dukais reef system (Fig. 1) on flows measured at the inner-plateau site.

Based on peak velocity magnitude, our study's most prominent event of strong sub-inertial flow is seen in the S2 and S3 velocity records during November–December 2010 (Figs. 4 and 11). This event of strong (>30 cm s^{-1}) northward flow begins on 15 November when the wind stress magnitude is weak (<0.05 Pa). It continues through the end of the velocity record (on 18 December) during which the alongshore wind is predominantly weak (<0.05 Pa) and directed to the south. A pulse of strong (>0.18 Pa) westward wind stress occurs during 27 November–5 December. However, as this follows the initiation of the strong northward current event by 12 d, it cannot be ascribed as a causative factor.

A mechanism that may be responsible for this, and other such flow events, is the interaction of basin eddies with the coastal region. Studies by Quadfasel and Baudner (1993) and Sofianos and Johns (2007) have shown that the central Red Sea basin is typically populated with eddies, encompassing velocities reaching 1 m s^{-1}. While assessing the influence of basin eddies on the coastal flow field is beyond the scope of this study, it is of interest to examine the basin eddy field during the time of the strong flow event described above and offer a hypothesis as to how this field may have influenced the flow in our study region.

Fields of SLA (Fig. 13) show two highly energetic eddies impinging on the eastern margin of the Red Sea basin near our mooring array during the November–December 2010 period of strong northward flow. One is an anticyclonic eddy, which over the period of roughly 12 November–8 December appears at the eastern basin margin north of the mooring array. After 8 December, it migrates to the northwest, away from the eastern margin. Over the 12 November–8 December period, offshore surface geostrophic currents of >15 cm s^{-1} associated with this feature are seen at the basin margin within 40 km of mooring array (Fig. 13a). Weaker onshore currents, associated with a second eddy appear in the surface geostrophic current field near the basin edge roughly 20 km south of the array. We hypothesize that the across-shore flow associated with these eddies may have set up an alongshore sea surface elevation gradient within the coastal zone, with higher elevation to the south and lower elevation to the north, which could have generated the northward flow seen at our moorings.

The surface geostrophic flow field associated with the second eddy, a cyclone, includes strong (>30 cm s^{-1}) onshore currents, which appear at the basin margin directly offshore of the mooring array over roughly 8–24 December (Fig. 13b). Again, we hypothesize that the localized across-margin flows associated with the eddy may have set up a coastal elevation gradient driving the northward flow seen at our mooring array.

4.9. The relative importance of low- and high-frequency motions in particle transport

It is of interest to assess the relative contribution of sub-inertial and higher-frequency flows in transporting material, such as fish and coral larvae, over our study region. The dominant higher-frequency signals (inertial-, diurnal- and semidiurnal-band motions)

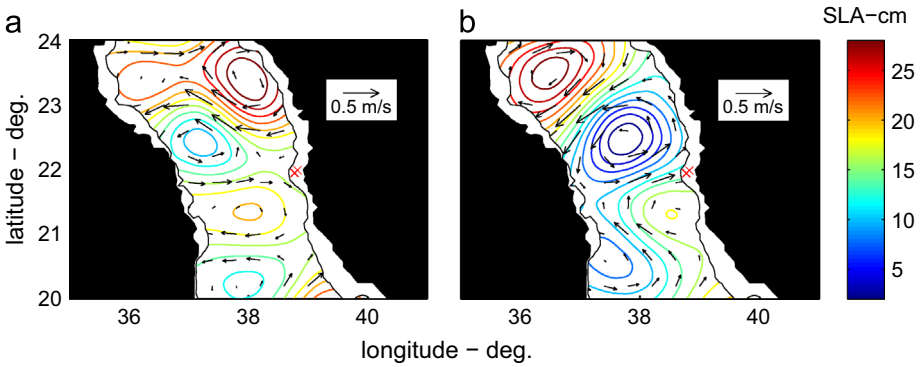

Fig. 13. Fields of sea level anomaly (SLA in cm) and surface geostrophic currents, computed from the SLA fields, for times (a - 17 November 2010, and b - 13 December 2010) encompassing the event of strong (>30 cm s^{-1}) northward flow observed at the outer and inner plateau moorings S1 and S3 (red x's). The SLA fields are not reliable, and are blanked out, in the area onshore of the 200-m isobath, marked by the black contours.

rotate at relatively short periods and so may be expected to result in smaller particle excursions than those associated with more slowly varying, sub-inertial, flow. To compare transport distances associated with sub-inertial and higher frequency currents, we have calculated particle displacements from high-pass (38-h half-power period) and low-pass (50-h half-power period) filtered velocity series (V_{hp} and V_{lp}, respectively; where V is the vector velocity). The displacements were calculated as

$$D(t_0) = \int_{t_0}^{t_0+T} V_F(t)dt$$

where t is time, V_F is the filtered velocity with mean removed and D is displacement over a period T (assuming a spatially homogeneous velocity field) of a particle set out at a time t_0. A displacement series was computed by stepping this integral through a velocity series. The relative importance of higher frequency motions in material transport was quantified as a ratio, R, of the root mean square of the displacements computed from V_{lp} to root mean square of the displacements computed from V_{hp}.

Values of R computed from the near-surface velocity records from the mid-plateau moorings S1 and S2, and for T in the range of 24–40 h, are of order 15 for N–S (alongshore) displacements and 7 for E–W displacements. R values tend to increase with increasing T beyond 40 h, reaching 57 and 26 for, respectively, N–S and E–W displacements at $T=5$ days. Sub-inertial flows may thus be regarded as the principal agent responsible for the transport of material over the mid-plateau. The relative importance of higher-frequency currents in material transport appears to be greater over the inner plateau. R values computed from the near-surface velocity record from S3, and with T in the 24–40 h range, are of order 9 for N–S displacements and 6 for E–W displacements.

5. Summary and conclusions

Our study area, a plateau adjacent to the Red Sea basin, is one of many different features of the bathymetrically complex Red Sea coastal zone (which includes fringing reefs and deep channels flanked by reef structures). Nevertheless, many of our findings may be deemed, with some caution, generally applicable to the coastal zone of the central Red Sea. Notably, tidal currents are particularly weak. The most energetic tidal constituent, the M_2 tide, has a magnitude of order 4 cm s^{-1} (Table 3). Semidiurnal-band currents, which include the S_2 tide and wind-forced flow, seldom exceed 8 cm s^{-1} (Fig. 10). Within the upper water column, currents in the diurnal and inertial bands are somewhat more energetic, with magnitudes occasionally in the 10–15 cm s^{-1} range (Fig. 10). These currents are surface intensified, particularly during times of strong vertical density stratification, and so appear to be principally wind-driven.

The frequent appearance of a diurnal warm layer associated with surface heating, which is seen during all seasons, is likely a principal factor limiting the correlation of the diurnal-band wind stress and near-surface currents (Section 4.6). As demonstrated by modeling and observational studies, the development of a diurnal warm layer complicates the wind-current relationship, as the near-surface thermal stratification influences the downward transfer of momentum imparted by wind and is itself influenced by wind-induced vertical mixing (Kondo et al., 1979; Price et al., 1986; Woods and Strass, 1986; Kawai and Wada, 2007; Noh et al., 2011).

Our calculations suggest that the transport of material over the mid-plateau is principally due to the sub-inertial flow, with higher frequency currents (periods <1.5 days) making a small contribution. The relative importance of higher frequency flows on material transport increases going to the inner plateau, raising the possibility that these flows may be of importance in transporting material in some near-shore environments.

Of particular significance is the indication that Red Sea basin eddies may be important in driving coastal flows. If so, the attendant exchange of coastal and basin water likely has a significant impact on coastal ecosystem, for example, in delivering nutrients from the basin to the coastal region or in moving coral and fish larvae offshore. In view of its potential importance to the Red Sea environment, we view the influence of basin flows on the coastal current field as a priority for further investigation.

Acknowledgments

For their work on the mooring deployment and recovery operations, our thanks go to the captains and crews of the *R/V Oceanus* as well as to C. Marquette, J. Kemp, J. Ryder, S. Whelan, J. Smith and P. Bouchard of the Woods Hole Oceanographic Institution (WHOI). Mooring fabrication was done by the WHOI Rigging Group. We are grateful to Dr. A. Al-Suwailem, H. Aljahdali, M. Aljahdali, R. Aljahdali, W. Almoazen, Captain E. Aravantinos and Y. Kattan of King Abdullah University of Sciences and Technology (KAUST) for providing logistical and field support. This research is based on work supported by Award nos. USA 00002 and KSA 00011 made by KAUST to WHOI.

References

Beardsley, R.C, Chapman, D.C., Brink, K.H., Ramp, S.R., Schlitz, R., 1985. The Nantucket Shoals flux experiment (NSFE79). Part I: a basic description of current and temperature variability. J. Phys. Oceanogr. 15, 713–748.

Chant, R.J., 2001. Evolution of near-inertial waves during an upwelling event on the New Jersey inner shelf. J. Phys. Oceanogr. 31, 746–764.
Chen, C., Reid, R.O., Nowlin , W.D., 1996. Near-inertial oscillations over the Texas-Louisiana shelf. J. Geophys. Res. 101, 3509–3524.
Churchill, J.H., 1985. Properties of flow within the coastal boundary layer off Long Island, New York. J. Phys. Oceanogr. 15, 898–916.
Colbo, K., Weller, R.A., 2009. Accuracy of the IMET sensor package in the subtropics. J. Atmos. Oceanic Technol. 26, 1867–1890.
Fairall, C.W., Bradley, E.F., Godfrey, J.C., Wick, G.A., Edson, J.B., Young, G.S., 1996. Cool-skin and warm-layer effects on sea surface temperature. J. Geophys. Res. 101, 1295–1308, http://dx.doi.org/10.1029/95JC03190.
Fairall, C.W., Bradley, E.F., Hare, J.E., Grachev, A.A., Edson, J.B., 2003. Bulk parameterization of air-sea fluxes: updates and verification for the COARE Algorithm. J. Climate 16, 571–591.
Gonella, J., 1972. A rotary-component method for analyzing meteorological and oceanographic vector time series. Deep-Sea Res. 19, 833–846.
Hosom, D.S., Weller, R.A., Payne, R.E., Prada, K.E., 1995. The IMET (Improved Meteorology) ship and buoy systems. J. Atmos. Oceanic Technol. 12, 527–540.
Jiang, H., Farrar, J.T., Beardsley, R.C., Chen, C., 2009. Zonal surface wind jets across the Red Sea due to mountain gap forcing along both sides of the Red Sea. Geophy. Res. Lett. 36, L19605, http://dx.doi.org/10.1029/2009GL040008.
Kawai, Y., Wada, A., 2007. Diurnal sea surface temperature variation and its impact on the atmosphere and ocean: a review. J. Oceanogr. 63, 721–744, http://dx.doi.org/10.1007/s10872-007-0063-0.
Kondo, J., Yasuhiro, S., Ishii, T., 1979. On wind-driven current and temperature profiles with diurnal period in the oceanic planetary boundary layer. J. Phys. Oceanogr. 9, 360–372.
Kundu, P.K., 1976. An analysis of inertial oscillations observed near the Oregon coast. J. Phys. Oceanogr. 6, 879–893.
Lentz, S.J., Churchill, J.H., Marquette, C., Smith, J., 2013. Evaluation and recommendations for improving the accuracy of an inexpensive water temperature logger. J. Atmosp. Oceanic Technol. 30, 1576–1582.
Lerczak, J.A., Hendershott, M.C., Winant, C.D., 2001. Observations and modeling of coastal internal waves driven by a diurnal sea breeze. J. Geophys. Res. 106, 19,715–19,729.
Limeburner, R., 1985. CODE-2: Moored array and large-scale data report. WHOI Technical Report 85–35, 234 pp.
Morcos, S.A., 1970. Physical and chemical oceanography of the Red Sea. Oceanogr. Mar. Biol. Annu. Rev. 8, 73–202.
Noh, Y., Lee, E., Kim, D.-H., Hong, S.-Y., Kim, M.-J., Ou, M.-L., 2011. Prediction of the diurnal warming of sea surface temperature using an atmosphere-ocean mixed layer coupled model. J. Geophys. Res. 116, C11023, http://dx.doi.org/10.1029/2011JC006970.
Pawlowicz, R., Beardsley, B., Lentz, S., 2002. Classical tidal harmonic analysis including error estimates in MATLAB using T_TIDE. Comput. Geosci. 28 (8), 929–937.
Payne, R.E., Anderson, S.P., 1999. A new look at the calibration and use ofEppley precision infrared radiometers Part II: Calibration and use of the Woods Hole Oceanographic Institution improved meteorology precision infrared radiometer. J. Atmos. Oceanic Technol. 16, 739–751.
Perkins, H., 1976. Observed effect of an eddy on inertial oscillations. Deep-Sea Res. 23, 1037–1042.
Price, J.F., Weller, R.A., Pinkel, R., 1986. Diurnal cycling: observations and models of the upper ocean response to diurnal heating, cooling, and wind mixing. J. Geophys. Res. 91, 8411–8427, http://dx.doi.org/10.1029/JC091iC07p08411.
Quadfasel, D., Baudner, H., 1993. Gyre-scale circulation cells in the Red Sea. Oceanol. Acta 16, 221–229.
Schumann, E., Perrins, L., 1982. Tidal and inertial currents around South Africa. Coastal Eng. Proc. 1 (18), http://dx.doi.org/10.9753/icce.v18.
Shearman, R.K., 2005. Observations of near-inertial current variability on the New England shelf. J. Geophys. Res. 110, C02012, http://dx.doi.org/10.1029/2004JC002341.
Smith, R.L., 1981. A comparison of the structure and variability of the flow field in three coastal upwelling regions: Oregon, northwest Africa, and Peru. In: Richards, F.A. (Ed.), Coastal Upwelling, Coastal and Estuarine Science, volume 1. AGU, Washington, D. C., pp. 107–118.
Sofianos, S.S., Johns, W.E., 2001. Wind induced sea level variability in the Red Sea. Geophys. Res. Lett. 28, 3175–3178.
Sofianos, S.S., Johns, W.E., 2007. Observations of the summer Red Sea circulation. J. Geophys. Res. 112, C06025, http://dx.doi.org/10.1029/2006JC003886.
Winant, C.D., Beardsley, R.C., Davis, R.E., 1987. Moored wind, temperature, and current observations made during Coastal Ocean Dynamics Experiments 1 and 2 over the northern California continental shelf and upper slope. J. Geophys. Res. 92, 1569–1604.
Woods, J.D., Strass, V., 1986. The response of the upper ocean to solar heating. II: The wind-driven current. Q. J. R. Meteorol. Soc., 112; , pp. 29–42.